Large-Scale Normal Coordinate Analysis of Macromolecular Systems: Thermal Properties of Polymer Particles and Crystals†

Kazuhiko Fukui,* Bobby G. Sumpter, and Donald W. Noid

Chemical and Analytical Sciences Division, Oak Ridge National Laboratory, Oak Ridge, Tennessee 37831-6197

Chao Yang

Computer Science and Mathematics Division, Oak Ridge National Laboratory, Oak Ridge, Tennessee 37831-6367

Robert E. Tuzun

Department of Compuational Science, State University of New York, Brockport, New York 14420

Received: September 7, 1999

Using novel modifications to a sparse matrix solver (ARPACK), a complete spectral analysis has been achieved for a 6000 atom polymer system involving all 18 000 degrees of freedom. A comparison of the thermal properties and spectra of an annealed polymer particle and crystal is presented. The density of states spectrum $g(\omega)$ shows a higher number of low-frequency modes for the polymer particle, which results in a higher heat capacity at low temperature. The distribution of energy level spacing shows some resemblance to that exhibited by random matrices. Finally, the displacement of low-frequency eigenvectors is shown to have a larger amplitude on the surface than in the interior of either the particle or crystal.

1. Introduction

Normal coordinate analysis (NCA) is an important tool to study spectral and thermal details of polymer processes at the atomic level. The reason for this is that once the spectral information has been obtained, it is very simple to link these observations to experimentally accessible macroscopic properties of polymeric materials. Although in the past normal mode calculations[1−9] have been limited to relatively small systems (i.e., ∼1000 atoms), new methods for diagonalizing large sparse matrices and the rapid increase in the available computer memory now allows routine calculation of much larger systems. Recently, a new computer method has been developed for the eigenanalysis of large sparse matrices to obtain a few eigenvalues. We have modified this method for the first time to obtain a complete set of frequencies needed to compute the density of states spectrum $g(\omega)$. We have chosen to illustrate this method with a comparison of the spectra and heat capacity for a polymer particle and crystal each with 6000 atoms (18 000 normal modes).

Polymer particles can be easily created in a recently developed experimental technique for creating very fine polymer particles of arbitrary composition and size.[10,11] In the experiment, we have used previously developed instrumentation for generation and characterization of droplet streams with small ($\leq 1-2\ \mu$m) average diameter and monodispersity for probing single molecules in solution.[12,13] This technique makes the initial volume of dilute solution sufficiently small so that the solvent evaporates on a short time scale. For micro- and nanoscale generated polymer particles, the refractive index is consistent with bulk (nominal) values, and the level of agreement with Mie theory indicates that the particles are nearly perfect spheres.[14] The particles in nano- and micrometer size range provide many unique physical properties since the size is below the point where critical length scales of physical phenomena become comparable to or larger than the size of the structure. Applications of such particles take advantage of high surface area and confinement effects, which lead to nanostructures with different properties than conventional materials.

A computational algorithm for generating and modeling polymer particles for our simulations was developed by constructing particles that are as similar as possible to the experimentally created polymer particles. Using this method we have examined a variety of PE nanoscale particles, allowing the systematic study of size-dependent physical properties of these particles.[15−18] The Hamiltonian models have been well tested and shown to provide a realistic representation of the structure and vibrational spectroscopy of a number of polymer systems: harmonic/Morse potentials for the bond stretches, harmonic potential for bending between two bonds, a truncated Fourier series for the torsional potential, and Lennard-Jones 6-12 potentials for the nonbonded interactions (both chain−chain and intrachain).[19−23] In the next section, we detail the methods and model used in our calculations, and the results are presented in section 3 followed by the conclusions of our study.

2. Methods and Model

The normal-mode analysis and molecular dynamics method are well-known methods based on classical mechanics and have been reviewed in several papers.[6,24−27] The standard normal-mode analysis methods involves solving the secular equation

$$|\mathbf{F} - \lambda\mathbf{I}| = 0 \qquad (1)$$

† Research sponsored by the Division of Materials Sciences, Office of Basic Energy Sciences, U.S. Department of Energy under contract DE-AC05-96OR22464 with Lockheed-Martin Energy Research Corp.

10.1021/jp993149+ CCC: $19.00
Published on Web 12/23/1999

where λ is the eigenvalue and **F** is the force constant matrix in mass-weighted Cartesian coordinates. The force matrix is obtained from the second derivative of potential function V,

$$\mathbf{F} = \mathbf{M}^{-1/2}(\nabla^2 V)\mathbf{M}^{-1/2} \tag{2}$$

where **M** is a diagonal mass matrix. These second derivatives were efficiently calculated analytically using methods described by Tuzun et al.[28−30] In our previous study, we have found that the traditional NCA methods for the calculation of the Hessian matrix results in large numbers of negative eigenvalues indicating many unstable degrees of freedom. To eliminate the negative eigenvalues, we use the time-averaged values of the Hessian **F** matrix obtained from molecular dynamics (MD). In our MD simulations, the integrations of the equations of motion, which requires the first derivative of the potential energy function, are carried out in Cartesian coordinates, thus giving an exact definition of the kinetic energy and coupling. These coupled equations are solved using novel symplectic integrators developed in our laboratory which conserve the volume of phase space and robustly allow integration for virtually any time scale.[31] A trajectory is created by specifying a low temperature ($\leq$0.1 K) in the system corresponding to an infinitesimal displacement of the atomic coordinate. Using an efficient formulation to calculate the analytical second derivatives of the internal coordinate along the trajectory, we evaluate the Hessian matrix every time step and obtain the averaged **F** matrix. A more detailed discussion of the properties for the matrix used in the present calculations can be found in ref 32.

2.1. Molecular Hamiltonian and Potential Energy Functions. For simplicity of the PE model, we have collapsed the CH_2 and CH_3 groups into a single particle (bead) of mass m = 14.5 amu. By neglecting the internal structure of those groups, we reduce the number of equations of motion for the system and can focus on the low-temperature effects as the hydrogens contribute little to the heat capacity, C_v. The MD simulations compute the momenta and coordinate of each atom in the system as a function of time by integrating Hamilton's equations of motion using the molecular Hamiltonian written in Cartesian coordinates. The total molecular Hamiltonian is composed of the kinetic, T, and potential energy, V, of the system,

$$H = \sum_{i=1}^{N} \frac{\mathbf{p}_i^2}{2m} + \sum V_{2b}(r_{i,i+1}) + \sum V_{3b}(\theta_{i,i+1,i+2}) + \sum V_{4b}(\tau_{i,i+1,i+2,i+3}) + \sum_{i=1}^{N-3}\sum_{j>i+3}^{N} V_{Nb}(r_{i,j}) \tag{3}$$

where N is a total number of atoms and $\mathbf{p}_i$ is the Cartesian momentum of the ith atom. r, θ, and τ are the internal coordinates for the interatomic distance, the bending angle between three consecutive atoms, and the torsional angle between four consecutive atoms, respectively. The potential energy functions have been demonstrated to yield good spectroscopic, thermodynamic, and kinetic data, as well as to provide the atomistic details of temperature-dependent phase transitions. The parameters for the potential energy in eq 3 are shown in Table 1.[33]

2.2. Generation of PE Polymer Particles and Crystals. We have developed an efficient method to obtain a desired size of the particles to model production of polymer particles for our MD simulations.[15,17,18] The procedure starts by preparing a set of randomly coiled chains with a chain length of 100 beads by propagating a classical trajectory with a perfectly planar all-trans zigzag initial conformation and randomly chosen momentum with a temperature of 300 K. The trajectory is terminated at 200 ps, and position and momenta of the chain are saved. By repeating this process, a desired set of randomly coiled chains is prepared. From this set, six chains are selected and placed along with Cartesian axis. We then create a collision at the Cartesian origin. These chains are propelled with an appropriate amount of momentum; then a particle consisting of the six chains is annealed to a desired temperature and rotated through a randomly chosen set of angles in three-dimensional space to generate a homogeneous particle. Another set of six chains is propelled at the particle to create another particle with 600 more atoms. This process is continued until the desired size of 6000 atoms is achieved for our study.

TABLE 1: Potential Parameters

stretch	$V_{2b} = {}^1/_2 k_r(r_{i,i+1} - r_0)^2$	
C−C	r_0	k_r
	1.53 Å	2651 kJ/mol
bending[a]	$V_{3b} = {}^1/_2 k_\theta(\cos\theta_{i,i+1,i+2} - \cos\theta_0)^2$	
C−C−C	θ_0	k_θ
	113°	130.1 kJ/mol
torsion	$V_{4b} = 8.77 + \alpha\cos\tau_{i,i+1,i+2,i+3} + \beta\cos^3\tau_{i,i+1,i+2,i+3}$	
C−C−C−C	α	β
	−18.41 kJ/mol	26.78 kJ/mol
nonbond	$V_{NB} = 4\epsilon[(\sigma/r_{ij})^{12} - (\sigma/r_{ij})^6]$	
$CH_2\cdots CH_2$	ϵ	σ
	0.494 kJ/mol	3.98 Å

2.3. Quasi Newton−Raphson Methods. Once the total potential energy has been described, a reasonable geometric structure for a particular molecule in Cartesian coordinates can be determined by using standard optimization techniques.[34] In the steepest descent method, the line search direction is defined along the direction of the local downhill gradient, $-\nabla V(x_i)$. Steepest descent can be quite inefficient, especially on energy surfaces having narrow valleys. More advanced algorithms are often designed to begin with a steepest-descent direction as the first step.

The reason that the steepest-descent method converges slowly near the minimum is that each segment of the path tends to reverse progress made in an earlier iteration. Successive line searches correct for this deviation, but they cannot efficiently correct because each direction must be orthogonal to the previous direction. Thus, the path oscillates and continually overcorrects for poor choices of directions in earlier steps. It would be preferable to prevent the next direction vector from undoing earlier progress. This means using an algorithm that produces a complete basis set of mutually conjugate directions such that each successive step continually refines the direction toward the minimum. If these conjugate directions truly span the space of the energy surface, then minimization along each direction in turn must by definition end in arriving at a minimum. The conjugate gradient algorithm constructs and follows such a set of directions.

Conjugate gradient is often the method of choice for large systems because, in contrast to Newton−Raphson methods, where a second-derivative matrix [$3N(N + 1)/2$] is required, only the previous $3N$ gradients and directions have to be stored. However, to ensure that the directions are mutually conjugate, more complete line search minimizations must be performed along each direction. Since these line searches consume several function evaluations per search, the time per iteration is longer for conjugate gradient than for steepest descent. This is more than compensated for by the smaller number of iterations.

The quasi-Newton−Raphson method follows the basic idea of the conjugate-gradient method by using the gradients of

previous iterations to direct the minimization along a more efficient pathway. However, the use of the gradients is within the Newton framework. In particular, a matrix **B** approximating the inverse of the Hessian ($\mathbf{A}^{-1}$) is constructed from the gradients using a variety of updating schemes. This matrix has the property that, in the limit of convergence, it is equivalent to $\mathbf{A}^{-1}$, so that, in this limit, the method is equivalent to the Newton−Raphson method. Another property of **B** is that it is always positive-definite and symmetric by construction, so that successive steps in the minimization always decrease the energy.

Of the several different updating schemes for determining **B**, one of the most common is the Broyden, Fletcher, Goldfarb, and Shanno (BFGS) algorithm.[34] Defining the changes in the coordinates and gradients for successive iterations, the approximate Hessians ($\mathbf{B}^{-1}$) are given by the following:

$$\mathbf{B}_{k+1} = \mathbf{B}_k + \left(1 + \frac{\delta^{\mathrm{T}}\mathbf{B}_k\delta}{\gamma^{\mathrm{T}}\delta}\right)\frac{\gamma\gamma^{\mathrm{T}}}{\gamma^{\mathrm{T}}\delta} - \frac{\gamma\delta^{\mathrm{T}}\mathbf{B}_k + \mathbf{B}_k\delta\gamma^{\mathrm{T}}}{\gamma^{\mathrm{T}}\delta} \quad (4)$$

In practice, the BFGS method is preferred over the other methods, because BFGS has been shown to converge globally with inexact line searches, while others have not.

The quasi-Newton−Raphson method has an advantage over the conjugate-gradients method in that it has been shown to be quadratically convergent for inexact line searches. Like the conjugate-gradients method, the method also avoids calculating the Hessian. However, it still requires the $N \times N$ disk space (N = number of atoms), and the updated Hessian approximation may become singular or indefinite even when the updating scheme guarantees hereditary positive-definiteness. Finally, the behavior may become inefficient in regions where the second derivatives change rapidly. Thus, this minimizer is often used as a bridge between the iterative Newton−Raphson and the conjugate-gradients methods.

2.4. Geometry Optimization of the PE Polymer Particles and Crystals. After the particle has been created, the geometry of the particle has to be optimized to create a reasonable equilibrium position for each of the 6000 atoms. By using a hybrid of the BFGS quasi-Newton minimization and simulated annealing via classical trajectories (periodically quenching the mementa, also known as dynamical steepest descent), the geometry of the particle and crystal could be quickly minimized to a reasonably low root-mean-square gradient: ~0.001. The resulting 6000 atom systems of the orthorhombic polyethylene crystal and the polymer particle are shown in Figure 1a,b, respectively. A single chain was chosen from the simulation of the crystal to obtain results for an isolated chain.

2.5. Solving the Secular Equation. The calculation of the full spectrum of a large sparse matrix is a challenging problem. A few possibilities follow.

1. Use dense eigenvalue calculation methods. These methods use orthogonal transformation to reduce **F** to a trigonal form first. They do not exploit the sparse structure of the matrix and require $O(n^2)$ storage, where n is the dimension of **F**. For a matrix of dimension 18 000, this amounts to about 2.6 GB memory (assuming the computation is done in 64-bit double precision)

2. Run n step Lanczos iteration[35] without saving all the Lanczos vectors. A k-step Lanczos process produces

$$\mathbf{F}\mathbf{V}_k = \mathbf{V}_k\mathbf{T}_k + \mathbf{f}_k\mathbf{e}_k^{\mathrm{T}} \quad (5)$$

where $\mathbf{T}_k$ is trigoanl, $\mathbf{V}_k T\,\mathbf{V}_k = \mathbf{T}_k$, and $\mathbf{V}_k T\,\mathbf{f}_k = 0$. Columns of $\mathbf{V}_k$ are referred to as Lanczos vectors. We will use $\mathbf{v}_j$ to denote the jth column of $\mathbf{V}_k$. In theory, each column of $\mathbf{V}_k$ can be generated by a three-term recurrence

$$\beta_j\mathbf{v}_{j+1} + \mathbf{F}\mathbf{v}_j - \beta_{j+1}\mathbf{v}_{j-1} - \alpha_j\mathbf{v}_j \quad (6)$$

Thus, one can reduce **F** to a tridiagonal form $\mathbf{T}_n$ at the cost of n matrix−vector multiplications and then use subroutines developed in LAPACK[36] to compute all eigenvalues of $\mathbf{T}_n$. However, it is well-known[37] that the Lanczos vectors generated by a three-term recurrence quickly become linearly dependent due to numerical roundoffs. As a consequence, eigenvalues of $\mathbf{T}_n$ may derive significantly from eigenvalues of **F**.

3. Split the spectrum of **F** into several intervals and use the implicit shifted Lanczos method (IRLM)[38] and spectral transformation to compute eigenvalues within each interval (see Figure 2.) This is the method we choose to use.

The implicitly restarted Lanczos method is implemented in ARPACK software.[39] It allows us to compute several eigenvalues using a small number of Lanczos basis vectors. Thus, the storage requirement of the Lanczos vector is moderate, and the cost for maintaining orthogonality between the Lanczos vector is low.

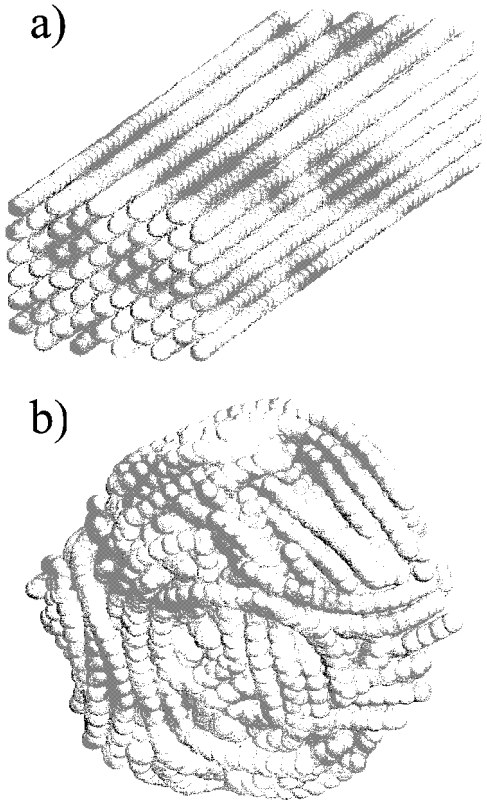

Figure 1. (a) Orthorhombic polyethylene crystal system containing 6000 atoms with a chain length of 100 beads. From the definition of an orthorhombic PE crystal, 60 chains of 100 atoms each were positioned in appropriate lattice positions. (b) Polyethylene particle for 6000 atoms with chain length of 100 beads. The diameter of the drops for 6000 atoms is 5.6 nm (determined from the averaged value of the distance from the center of mass to the surface atoms).

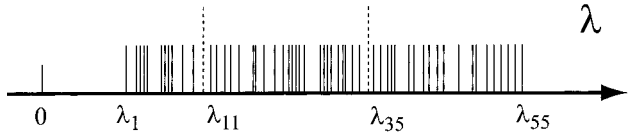

Figure 2. Splitting of spectrum into several intervals. Within each interval, shifted and inverted Lanczos runs are performed to capture all desired eigenvalues.

Spectral transformation is used to improve the convergence of the interior and clustered eigenvalues. Instead of computing eigenvalues of **F** directly, we compute eigenvalues of $(\mathbf{F} - \sigma\mathbf{I})^{-1}$, where σ is our target shift. (We are interested in eigenvalues nearest to σ.) Under the transformation, $\psi(\lambda) = 1/(\lambda - \sigma)$, the interior and clustered eigenvalues of **F** become dominant eigenvalues of $(\mathbf{F} - \sigma\mathbf{I})^{-1}$. They tend to converge rapidly in the Lanczos process. Note eigenvectors are invariant under this transformation. An eigenvalue μ of the transformed problem can be converted to an eigenvalue of the original problem by

$$\lambda = \sigma + \frac{1}{\mu} \tag{7}$$

Spectral transformation requires factoring the sparse matrix $\mathbf{F} - \sigma\mathbf{I}$ into a product of $\mathbf{LDL}^{\mathrm{T}}$, where **L** is the unit lower triangular and **D** is diagonal. The matrix−vector multiplication in the original Lanczos iteration is replaced by sparse triangular solutions. Sparse matrix factorization takes a significant amount of computational resources.

The main challenge of our approach is to decide how to partition the spectrum. Since the calculation of all eigenvalues within one interval requires a relatively expensive sparse matrix factorization, we do not want to divide the spectrum into many small intervals. On the other hand, if an interval is too large and contains too many eigenvalues, the convergence of IRLM on that interval may be very slow, causing overall performance degradation.

Heuristics are developed in ref 40 to minimize the average cost for computing one eigenvalue. These heuristics are slight modifications to the earlier work done.[41] The main ingredients of these heuristics are

1. careful evaluation of the total cost associated with IRLM
2. accurate prediction of the number of eigenvalues that are going to converge in the next step of IRLM

The details of these heuristics are beyond the scope of this paper. The reader may see refs 40 and 41 for more details.

In our experiment, we set the first target shift at $\sigma = -0.05$, and let IRLM comute the lowest 100 eigenvalues. The first run is terminated when all 100 desired eigenvalues have converged or when the average cost for computing one eigenvalue becomes too high. Upon the termination of the first run, a new target shift is chosen (our heuristic chooses it to be the midpoint between the last converged eigenvalue and the estimation of the next eigenvalue), the matrix $\mathbf{F} - \sigma\mathbf{I}$ is factored again, and a new IRLM run begins to compute eigenvalues to the right of the new shift. This process continues until all eigenvalues are found.

3. Results

3.1. Spectral Properties of Polymer Particles and Crystals. Using the methods described above, we calculate complete frequency spectra $g(\omega)$ for 100 atoms of a single chain and 6000 atoms of the crystal and particle systems. Figure 3 contrasts the resulting frequencies for 3 systems in units of cm^{-1} obtained from the averaged (solid lines) and single (dotted line) Hessian. The standard method to evaluate the Hessian matrix would be to choose a single configuration to evaluate all of the terms of the matrix. For the single configuration case, the crystal systems had 38 negative eigenvalues while the particle had 71 negative ones out of the 17 994 values to be expected (the 3 translations and 3 rotational modes are eliminated). Using the molecular dynamics to average the Hessian over 50 ps, we obtain only 1 negative eigenvalue for the crystal and no negative ones for the particle. The lowest vibrational modes are 2.5 and 2.3 cm^{-1} for the particle and crystal, respectively. As can be easily seen, the resulting plots of the histogram of the spectral frequencies $g(\omega)$ are similar and have sharp cutoffs at very near the same frequency. On closer inspection, noticeable differences are found in the shape of $g(\omega)$ at near $\omega \rightarrow 0$ compared with the single chain. Furthermore, the low-frequency band is flatter for the particle as compared to the crystal. A sharp peak appears in the middle of the high-frequency band for the particle and is not found for the crystal or single chain. Another way of examining the spectra is to investigate the distribution of $P(s)$ of the spacings of neighboring eigenvalues. This distribution can be compared to a Poisson (exponential distribution) and to Wigner (Gaussian ensemble) law.[42] The plot for the histogram of the spacings $P(s)$ is presented in Figure 4. Both $P(s)$ values seem to be of Wigner distribution type and not the Poison distribution, which increases near $s = 0$. This may indicate that the spectra has some features similar to a random matrix, presumably due to somewhat random fluctuations in the interactions encountered.[43]

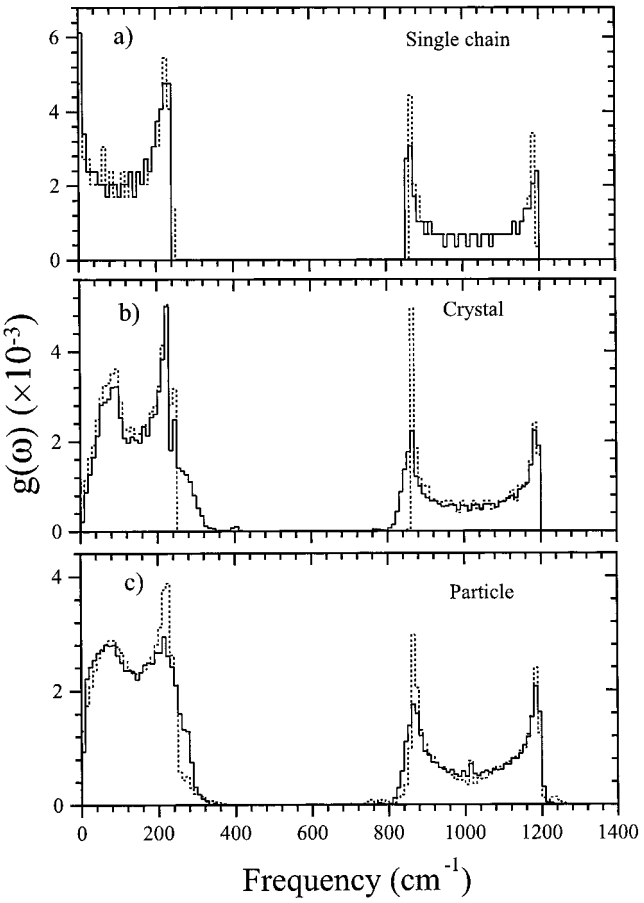

Figure 3. Histograms of the normalized spectral frequencies of (a) a single chain (a perfectly planar all-trans zigzag conformation) and (b) a crystal and (c) a particle with a chain length of 1000 beads. The spectral frequencies $g(\omega)$ obtained from averaging the Hessian are shown as solid lines, and the dotted lines are the spectra calculated from the single configuration. For the spectra of crystal and particle systems in the single configuration, 38 and 71 negative eigenvalues are obtained out of the 17 994 values (the 3 translations and 3 rotational modes are eliminated). The negative frequencies are added in the first bin of the histogram (dotted lines).

3.2. Eigenvectors of Polymer Particles and Crystals. The eigenvectors **A** obtained from the secular eq 1 contain the amplitudes A_{ik} for each atom in Cartesian coordinates of the normal modes k. A plot of the values of the displacement

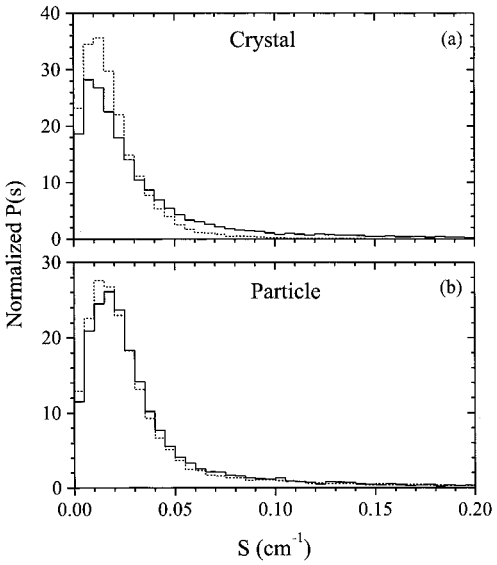

Figure 4. Histogram of the spacings for (a) crystal and (b) particle systems. The normalized distribution $P(s)$ is obtained from the differences between two consecutive eigenvalues $s_i = \omega_{i+1} - \omega_i$. The solid and dotted lines are calculated from the eigenvalues obtained from the averaged and single Hessian, respectively.

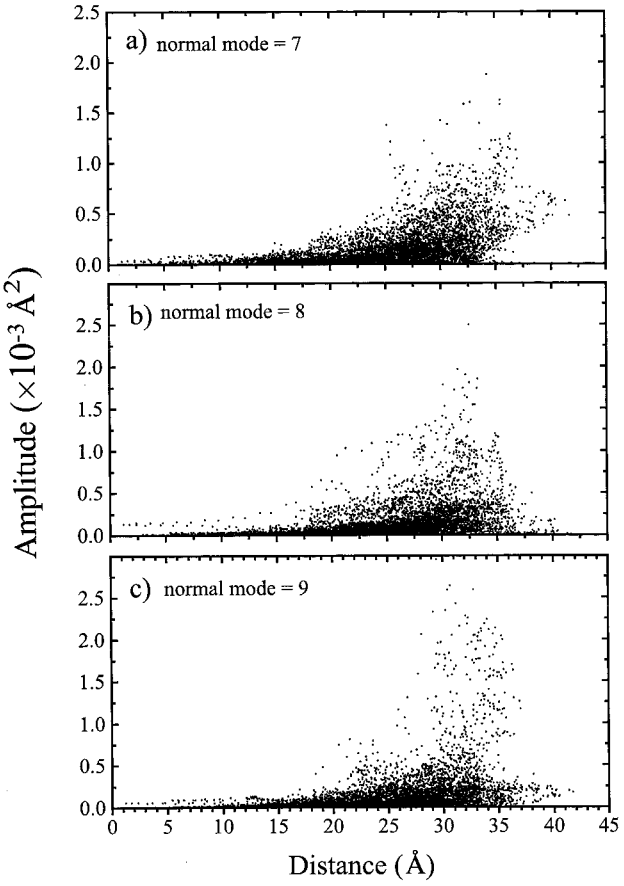

Figure 5. Displacement of normal modes as a function of the distance from the PE particle center: (a) for normal mode 7; (b) for normal mode 8; (c) for normal mode 9. Note that the modes from 1 to 6 are rotational and translational modes.

$(A_{xk}^2 + A_{yk}^2 + A_{zk}^2)$ as a function of the distance from the center of particle [the particle was centered so that the center of mass is at (0,0,0)] is presented in Figure 5. Because this particle mode has some similarity with modes of an elastic sphere, it was expected that a much larger amplitude will be found for surface atoms.

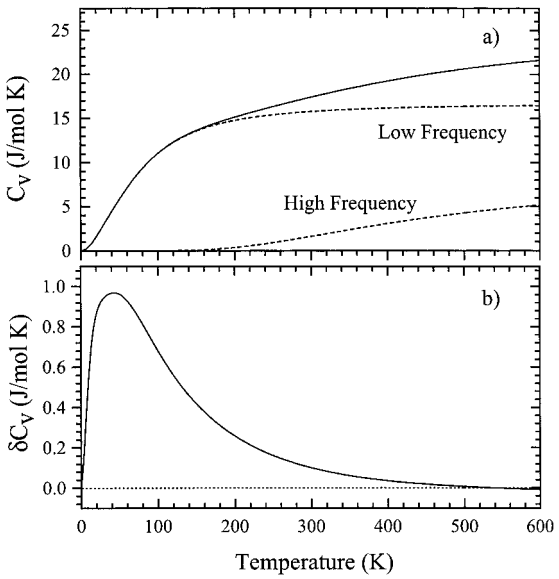

Figure 6. (a) Dependence of heat capacity on temperature for a 6000 atom PE crystal. The dashed lines are calculated from the high- and low-frequency regions (see Figure 3). (b) Comparison of heat capacity between the PE crystal and particle. The difference of C_v is defined as $\delta C_v = C_v(\text{particle}) - C_v(\text{crystal})$.

3.3. Thermal Properties of Polymer Particles and Crystals. The heat capacity of particles and crystals at low temperature can easily be calculated from the $g(\omega)$ using the equation[44]

$$C_v = k_B \int_0^\infty \frac{(h\omega c/k_B T)^2 e^{-h\omega c/k_B T} g(\omega)\, d\omega}{(1 - e^{-h\omega c/k_B T})^2} \qquad (8)$$

where k_B is Boltzmann's constant, c is the speed of light, h is Planck's constant, and ω is the frequency in cm^{-1}. Figure 6a shows the temperature dependence for C_v for the temperature range 0−600 K for the crystal. From Figure 3, we can distinguish two separate frequency regions: high- and low-frequency modes. The low-frequency modes can be described as a torsional and accordion-like S motion of the CH_2 backbone, which is from the bending of the $CH_2-CH_2-CH_2$ bonds on compression of the chain followed by extension. These motions contribute mainly to the increase in heat capacity from 0 to 200 K. The motions of higher frequencies involve CH_2-CH_2 stretching vibration, not coupled sufficiently with the chain, and contribute to C_v above 200 K.[45] A comparison of the corresponding values of C_v subtracting from the crystal is in the accompanying plot Figure 6b. The increase of C_v for the particle at the low temperature is presumably due to the increase of the density of states at low values of $g(\omega)$.

4. Summary and Conclusions

Novel modifications to the sparse matrix solver (ARPACK) allowed us for the first time to perform a complete spectral analysis for a 6000 atom polymer particle and crystal involving all 18 000 degrees of freedom. We determined accurate vibrational spectra by averaging the terms of the Hessian matrix (second derivatives of the energy function) over a short trajectory so that the unstable modes were completely eliminated for the 6000 atom model polymer particles and crystals. The density of states spectrum $g(\omega)$ shows a higher number of low-frequency modes for a polymer particle, which results in a higher heat capacity at low temperature. The heat capacity calculated from the density of states for the particle and crystal systems shows that the low-frequency modes, such as torsional and

accordion-like S motion of the CH_2 backbone, contribute mainly to the increase in heat capacity from 0 to 200 K, while the high-frequency modes, such as CH_2-CH_2 stretching motion, contribute to that above 200 K. The increase of the low-temperature C_v is presumably due to the increase of the density of states at low values of the $g(\omega)$.

Analysis of the eigenvalues shows a distribution of energy level spacing that resembles that exhibited by random matrices, suggesting that the eigenvalue calculation may have increased sensitivities to the parameters used. Finally, as expected, the particle modes have some similarity with modes of an elastic sphere, where much larger amplitudes are found for the surface atoms.

Acknowledgment. K.F. is supported by the Postdoctoral Research Associates Program administered jointly by fellowship at Oak Ridge National Laboratory (ORNL) and Oak Ridge Institute for Science and Education, and C.Y. was supported in part by a Householder fellowship at ORNL. We thank NEC for assistance in using the NEC SX-4 supercomputer.

References and Notes

(1) Painter, P. C.; Coleman, M. M.; Koenig, J. L. *The Theory of Vibrational Spectroscopy and Its Application to Polymeric Materials*; Wiley: New York, 1982.
(2) Snyder, R. G.; Hso, S. L.; Krimm, S. *Spectrochim. Acta* **1963**, *19*, 85.
(3) Snyder, R. G.; Strauss, H. L. *J. Chem. Phys.* **1987**, *87*, 3779.
(4) Krimm, S.; Liang, C. Y.; Sutherland, G. B. *J. Chem. Phys.* **1956**, *25*, 549.
(5) Mazur, J.; Reneker, D. H.; Granconi, B. M. *Polym. Commun.* **1987**, *28*, 78.
(6) Brooks, B.; Janezic, D.; Karplus, M. *J. Comput. Chem. Phys.* **1995**, *16*, 1522.
(7) van Vlijmen, H. W. T.; Karplus, M. *J. Phys. Chem. B* **1995**, *103*, 3009.
(8) Grafton, A. K.; Wheeler, R. A. *J. Comput. Chem. Phys.* **1995**, *19*, 1663.
(9) Murry, R. L.; Fourkas, J. T.; Li, W.-X.; Keyes, T. *J. Chem. Phys.* **1999**, *110*, 10410.
(10) Kung, C.-Y.; Barnes, M. D.; Sumpter, B. G.; Noid, D. W.; Otaigbe, J. U. *Polym. Prepr. (Am. Chem. Soc., Div. Polym. Chem.)* **1999**, *39*, 610.
(11) Barnes, M. D.; Kung, C.-Y.; Lermer, N.; Fukui, K.; Sumpter, B. G.; Noid, D. W. *Opt. Lett.* **1999**, *24*, 121.
(12) Kung, C.-Y.; Barnes, M. D.; Lermer, N.; Whitten, W. B.; Ramsey, J. M. *Anal. Chem.* **1998**, *70*, 658.
(13) Barnes, M. D.; Lermer, N.; Kung, C.-Y.; Whitten, W. B.; Ramsey, J. M. *Opt. Lett.* **1997**, *22*, 1265.
(14) Barnes, M. D.; Lermer, N.; Whitten, W. B.; Ramsey, J. M. *Rev. Sci. Instrum.* **1997**, *68*, 2287.
(15) Fukui, K.; Sumpter, B. G.; Barnes, M. D.; Noid, D. W.; Otaigbe, J. U. *Macromol. Theory Simul.* **1999**, *8*, 28.
(16) Fukui, K.; Sumpter, B. G.; Runge, K.; Kung, C.-Y.; Barnes, M. D.; Noid, D. W. *Chem. Phys.* **1999**, *244*, 339.
(17) Fukui, K.; Sumpter, B. G.; Barnes, M. D.; Noid, D. W. *Comput. Theor. Polym. Sci.* **1999**, *9*, 245.
(18) Fukui, K.; Sumpter, B. G.; Barnes, M. D.; Noid, D. W. *Polym. J.* **1999**, *8*, 664.
(19) Jin, Y.; Boyd, R. H. *J. Chem. Phys.* **1998**, *108*, 9912.
(20) Roy, R.; Sumpter, B. G.; Pfeffer, G. A.; Gray, S. K.; Noid, D. W. *Phys. Rep.* **1991**, *205*, 109.
(21) Roy, R.; Sumpter, B. G.; Noid, D. W.; Wunderlich, B. *J. Phys. Chem.* **1990**, *94*, 5729.
(22) Sumpter, B. G.; Noid, D. W.; Wunderlich, B. *Polymer* **1990**, *31*, 1254.
(23) Sumpter, B. G.; Noid, D. W.; Wunderlich, B.; Cheng, S. Z. D. *Macromolecules* **1990**, *23*, 4671.
(24) Hoover, W. G. *Annu. Rev. Phys. Chem.* **1983**, *34*, 103.
(25) Klein, M. L. *Annu. Rev. Phys. Chem.* **1985**, *36*, 525.
(26) Wilson, E. B.; Decius, J. C.; Cross, P. C. *Molecular Vibrations*; McGraw-Hill: New York, 1955.
(27) Meister, A. G.; Clevel, F. F. *Am. J. Phys.* **1946**, *14*, 13.
(28) Tuzun, R. E.; Noid, D. W.; Sumpter, B. G. *Macromol. Theory Simul.* **1996**, *5*, 771.
(29) Tuzun, R. E.; Noid, D. W.; Sumpter, B. G. *J. Comput. Chem.* **1997**, *18*, 1804.
(30) Tuzun, R. E.; Noid, D. W.; Sumpter, B. G. *J. Comput. Chem.* **1997**, *18*, 1513.
(31) Gray, S. K.; Noid, D. W.; Sumpter, B. G. *J. Chem. Phys.* **1994**, *101*, 4062.
(32) Noid, D. W.; Fukui, K.; Sumpter, B. G.; Yang, C.; Tuzun, R. E. *Chem. Phys. Lett.*, in press.
(33) Boyd, R. H.; Breitling, S. M. *Macromolecules* **1974**, *7*, 855.
(34) Fletcher, R. *Practical Methods of Optimization*; John Wiley & Sons: New York, 1987.
(35) Lanczos, C. *J. Res. Natl. Bur. Stand.* **1950**, *45*, 255.
(36) Anderson, E.; et al. *LAPACK Users Guide*; SIAM: Philadelphia 1995.
(37) Parlett, B. N. *The symmetric Eigenvalue Problem*; Prentice-Hall: Englewood Cliffs, NJ, 1980.
(38) Sorensen, D. C. *SIAM J. Matrix Analysis Applications* **1992**, *13*, 357.
(39) Lehoucq, R. B.; Sorensen, D. C.; Yang, C. *ARPACK Users' Guide-Solution of Large-scale eigenvalue problems with implicitly restarted Arnoldi Methods*; SIAM: Philadelphia, 1999.
(40) Yang, C. Accelerating the Arnoldi Iteration-Theory and Practice. Ph.D. Thesis, Department of CAAM, Rice University, Houston, TX, 1998.
(41) Grimes, R. G.; Lewis, J. G.; Simon, H. D. *SIAM J. Matrix Analysis Applications* **1994**, *15*, 228.
(42) Meyer, H.; d'Auriac, J.-C. *Phys. Rev. E* **1997**, *55*, 5380.
(43) Meyer, H.; d'Auriac, J.-C.; Bruus, H. *J. Phys. A: Math. Gen.* **1996**, *29*, 483.
(44) McQuarrie, D. A. *Statistical Mechanics*; Haper & Row: New York, 1976.
(45) Wunderlich, B. *Thermal Analysis*; Academic Press: San Diego, 1990.